Sensors & Actuators: B. Chemical 444 (2025) 138459

Contents lists available at ScienceDirect

Sensors and Actuators: B. Chemical

journal homepage: www.elsevier.com/locate/snb

A modularized chemical species tomography sensor for dynamic imaging of gas-turbine exhaust

Minqiu Zhou [a], Rui Zhang [a], Yikai Xia [a], Yuan Chen [a], Ihab Ahmed [b], Mohamed Pourkashanian [b], Ian Armstrong [c], Michael Lengden [c], Walter Johnstone [c], Hugh McCann [a], Chang Liu [a,*]

[a] Institute for Imaging, Data and Communications, School of Engineering, The University of Edinburgh, Edinburgh EH9 3JL, UK
[b] Department of Mechanical Engineering, The University of Sheffield, Sheffield S10 2TN, UK
[c] Department of Electronic and Electrical Engineering, University of Strathclyde, Glasgow G1 1XQ, UK

ARTICLE INFO

Keywords:
Chemical species tomography
Laser absorption spectroscopy
Gas turbine
Exhaust gas temperature
Water vapor concentration

ABSTRACT

Chemical Species Tomography (CST) has been widely used for spatiotemporal resolution of gas-state parameters, such as species concentration and temperature, in harsh reactive-flow environments, such as gas-turbine exhaust plumes. To enhance adaptability across gas turbines of varying scales, we introduce a novel modularized CST architecture, where each individual laser beam in the tomographic array is implemented by a compact emitter-receiver unit, and the signal from the transmitted beams are digitized and collected by a bespoke high-speed data acquisition system. In this work, we present a CST sensor with 128 emitter-receiver units, i.e., 128 laser beams, arranged into four equi-angular projections, each with 32 equi-spaced parallel laser beams. Our miniaturized opto-mechanical and opto-electronic design reduces beam spacing to 10 mm, achieving a spatial resolution of 8.1 mm with the 128-beam tomographic layout. The laser transmissions are detected, conditioned and digitized by a 128-channel data acquisition system, enabling instantaneous imaging of water vapor concentration and temperature at 250 frames per second. To validate the CST sensor, we conducted lab-scale experiments on partially premixed propane/air flames, demonstrating good agreement between the reconstructed images and the real flames, in terms of both gas-state profiles and dynamics. The CST sensor was deployed to reconstruct, for the first time, the water vapor concentration and temperature fields within the exhaust plume of a commercial gas turbine, viz. a Honeywell 131–9 A Auxiliary Power Unit. The images show clearly the non-uniform gas-state distributions that were designed specifically to assess the efficacy of the CST sensor. This modularized CST sensor offers a versatile and scalable solution for gas-turbine exhaust diagnosis, providing critical insights into engine performance and fault diagnosis.

1. Introduction

Chemical Species Tomography (CST) is a robust imaging technique that enables non-intrusive and fast reconstruction of gas-state fields, such as species concentration, temperature and velocity, in reactive flows [1–6]. By using multiple laser beams and tomographic algorithms, CST provides spatially and temporally resolved flow-field measurement in the aviation, marine, and power generation sectors. Stringent requirements for emission reduction in these sectors have placed increasing emphasis on accurate diagnostics of combustion processes. Understanding the spatiotemporal characteristics of exhaust gases, particularly temperature and species concentration, is essential for assessing engine performance, validating emission models, and supporting health monitoring of gas turbines. Conventional exhaust diagnostics rely on extractive sampling, which suffers from limited sensitivity and spatial resolution, and lacks temporal information due to offline analysis [7,8]. In contrast, non-intrusive imaging techniques such as CST can directly reveal spatial inhomogeneities and transient features in the exhaust, providing insights into incomplete combustion, injector malfunctions, or fuel-air mixing issues [9]. These capabilities are particularly relevant in modern low-emission combustor designs, where flame stability and lean blow-out are critical challenges [8].

The sensor design of a CST system for gas-turbine exhaust imaging presents significant challenges due to the harsh test environment, in

* Corresponding author.
E-mail address: c.liu@ed.ac.uk (C. Liu).

https://doi.org/10.1016/j.snb.2025.138459
Received 29 April 2025; Received in revised form 19 July 2025; Accepted 2 August 2025
Available online 6 August 2025

which the exhaust plume exhibits high temperature, i.e. 300–800 °C, and high velocity, 30–150 m/s, and the level of acoustic noise can reach up to 135 dB. Such testing environment requires a robust CST sensor that can withstand thermal stress, vibration, and contamination from exhaust particulates. In addition, the diameter near the exhaust nozzle of an Auxiliary Power Unit (APU) is 0.2–0.6 m [10], while that of a main propulsion aero-engine can be 1–2 m [7]. The various engine dimensions require the CST sensor to be accordingly sized up and down to resolve the target exhaust plume with sufficient resolution, and preferably without complete re-design of key hardware, i.e. laser emitter-receiver units.

Design of laser emitter-receiver units in a CST sensor requires customised optics to launch and collimate the laser beam, opto-mechanics to align and fix the laser beam, and opto-electronics to receive and amplify the laser signal. Emitter-receiver strategies reported previously are based on either fan-shaped laser sheets or individual laser beams [11]. The former, generally achieved by planar expansion of several collimated laser beams, has insufficient power to cover large-size target flows [8,12]. In contrast, the latter strategy can be flexibly arranged in the sensing region, thus enabling adaptation to target flows with various sizes. To date, Wang et al. developed a sensor with 12 laser beams to image the two-dimensional (2D) fields of temperature and water vapor concentration in the exhaust of a diesel-fuelled small turbojet engine. Although a high temporal resolution of 20 kHz is achieved, the spatial resolution is severely limited. Ma et al. utilized two orthogonal projections of 30 parallel beams to image the J85 exhaust [13], however, such beam arrangement is incapable of resolving nonuniform and asymmetric target [1]. To achieve a better spatial resolution, Zhao et al. arranged 100 multi-angle laser beams to finely resolve the temperature fields at the outlet of an afterburner test rig [14]. In addition, Upadhyay et al. [7] designed a large-size CST sensor with 126 laser beams, each traversing a 7-meter path, to resolve the carbon dioxide emissions in the exhaust plume (estimated to be 1.5 m in diameter) of a Rolls-Royce modern Trent engine. However, both of the latter two sensors have optical components that were customised to match the size of the target flow. In case of applying to a different-size engine, a major rework on the hardware will be unavoidable. Since more than 100 laser beams were sequentially sampled, both sensors also suffer from slow temporal responses, e.g., up to 1–2 frames per second.

To address the above challenges, this paper introduces a novel modularized CST architecture, where each laser beam in the tomographic layout is implemented by an individual, compact emitter-receiver unit. This new architecture offers a versatile and scalable solution for CST-based gas-turbine exhaust diagnosis, since the multiple emitter-receiver units only need to be rearranged on a tomographic frame of larger diameter and with larger beam spacing, without any further hardware modification. It also facilitates maintenance of the CST sensor in industrial practice, in which each laser-beam can be replaced and tested independently. The main contributions of this paper are:

1. A 128-beam modularized CST sensor is designed, enabling a spatial resolution of 8.1 mm with miniaturized but versatile opto-mechanical and opto-electronic components. The modularized sensor, combined with our high-speed channel-reconfigurable data acquisition system [15], achieves dynamic gas-state imaging at 250 frames per second.

2. A lab-scale experiment is carried out to validate the performance of the modularized sensor in reconstructing water vapor concentration and temperature distributions in post-combustion flow fields with various profiles and dynamics. We quantify uncertainties in localizing hot spots and determining their size, as well as examining the pulsations of the turbulent flows.

3. The designed sensor is deployed to dynamically reconstruct, for the first time, the water vapor concentration and temperature fields within the exhaust plume of a commercial gas turbine, a Honeywell APU. The industrial experiment is designed to create non-uniform gas-state distributions in the exhaust plume, in order to evaluate the efficacy of the CST sensor.

The rest of the paper is organized as follows. In Section 2, the principles of CST are introduced. The modularized sensor design is detailed in Section 3. Section 4 presents the lab-scale experiment and quantification of the sensor performance on flow-field imaging. Section 5 describes application of the developed sensor to imaging of the APU exhaust plume. The paper is concluded in Section 6.

2. Principles of CST

This section briefly summarizes the mathematical background of CST; a more thorough treatment is presented in [1]. When a laser beam at a species-absorbing wavenumber ν [cm^{-1}] penetrates through target gas, the absorbance $\alpha(\nu)$ can be expressed using the Beer-Lambert law [16,17] as:

$$\alpha(\nu) = -\ln\frac{I_0(\nu)}{I_t(\nu)} = \int_0^L P(l)\chi(l)S(T(l))\phi(\nu,l)dl, \tag{1}$$

where $I_0(\nu)$ and $I_t(\nu)$ are the incident and the transmitted laser intensities, respectively. $P(l)$ [atm] is the local pressure at l [cm]. $\chi(l)$ is the mole fraction of the absorbing species. For each absorbing transition of the target species, the line strength $S(T(l))$ [cm^{-2}•atm^{-1}] is a function that is dependent on temperature $T(l)$ [K]. The total path length of the laser beam is denoted by L [cm]. The absorbance lineshape function $\phi(\nu,l)$ of each absorbing feature satisfies the condition $\int_{-\infty}^{+\infty}\phi(\nu,l)d\nu \equiv 1$. Therefore, the line-of-sight (LoS) path-integrated absorption A_ν can be written as:

$$A_\nu = \int_{-\infty}^{+\infty}\alpha(\nu)d\nu = \int_0^L [P(l)\chi(l)S(T(l))]dl = \int_0^L a(\nu,l)dl, \tag{2}$$

where $a(\nu,l)$ is the local absorption density. Fig. 1 shows a LoS measurement in a CST sensing region. The Region of Interest (ROI) is divided into M grid cells, while the area outside the ROI is regarded as the ambient background. Within each grid cell, the gas parameters, e.g. P, T, χ are assumed to be uniform. Consequently, the LoS measurement is also discretized linearly, allowing us to formulate the CST signal as:

$$A_{\nu,n} = A_{\nu,n}^{ROI} + A_{\nu,n}^{ambient} = \sum_{m=1}^{M} L_{n,m}^{ROI} a_{\nu,n,m}^{ROI} + L_n^{ambient} a_{\nu,n}^{ambient} \tag{3}$$

where $A_{\nu,n}$ is measured path-integrated absorption of the n-th laser beam at wavenumber ν, a summation of that in the ROI $A_{\nu,n}^{RoI}$ and in the ambient $A_{\nu,n}^{ambient}$. $L_{n,m}^{ROI}$ denotes the segmental laser path of n-th laser beam in the m-th grid cell. The absorption density in the m-th ($m \in 1, 2, \ldots, M$) grid is denoted as $a_{\nu,n,m}^{ROI} = P_m\chi_m S(T_m)$. $L_n^{ambient}$ and $a_{\nu,n}^{ambient}$ denote the length of laser path and absorption density in the ambient region, respectively. A matrix form of Eq. (3) can be written as:

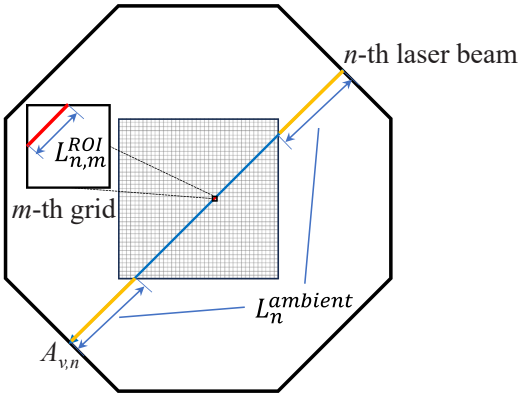

Fig. 1. Geometric layout of a LoS measurement in CST.

$$\boldsymbol{A}_v = \boldsymbol{L}\boldsymbol{a}_v, \tag{4}$$

where $\boldsymbol{A}_v \in \mathbb{R}^{N\times 1}$ is the vector of path-integrated absorption from N laser beams. $\boldsymbol{L} \in \mathbb{R}^{N\times(M+1)}$ is the sensitivity matrix. $a_v \in \mathbb{R}^{1\times(M+1)}$ is the vector of absorption density in all M grid cells. The spectroscopic method adopted is discussed further in Section 3.1, but it's important to note at this point that the wavelength of the emitted laser light is scanned in order to cover selected absorption features of the target species.

In industrial practice, the limited optical access, e.g., subject to safe operation of the combustion systems, generally restricts the number of LoS measurements to less than 150 [11]. That is, the CST inverse problem for large values of M suffers from a significant rank deficiency. As a result, direct inversion methods used in computer tomography, such as Linear Back Projection, typically amplify measurement noise in the reconstructed images. As a popular inversion method used in process tomography, Tikhonov regularization is computationally efficient and generally produces reasonable results by imposing spatial smoothness [5,18,19], and therefore, is adopted in this work. The Tikhonov regularization is achieved by the following minimization:

$$\widehat{\boldsymbol{a}_v} = \underset{\boldsymbol{a}_v}{\operatorname{argmin}} \|\boldsymbol{A}_v - \boldsymbol{L}\boldsymbol{a}_v\|_2^2 + \lambda\|\boldsymbol{F}\boldsymbol{a}_v\|_2^2 \tag{5}$$

where $\boldsymbol{F}$ is the discrete Laplacian. Minimizing $\|\boldsymbol{F}\boldsymbol{a}_v\|_2^2$ with the data fidelity term $\|\boldsymbol{A}_v - \boldsymbol{L}\boldsymbol{a}_v\|_2^2$ contributes to smooth solutions. The regularization parameter λ is chosen using the L-curve method [18] which balances the data fidelity and smoothness.

3. Sensor design

The CST system consists of 128 emitter-receiver units, i.e., 128 laser beams, arranged into four equi-angular projections with 32 equi-spaced parallel laser beams per projection. In the following, we detail the design of the modular emitter-receiver unit, their assembly for the CST sensor, and the data acquisition system to digitize the transmitted laser signals.

3.1. Modular emitter-receiver unit design

Fig. 2 depicts the modularized CST sensor developed for this work. The emitter unit mainly consists of a fiber-coupled C-lens collimator, a right-angle prism, an adjustable mirror mount and a base frame [20]. The C-lens collimator is made of oxide glass and anti-reflection (AR) coated to enable transmittance of more than 97 % in the wavelength range of 1250–1650 nm, covering the water vapor absorbing transitions at 1391 nm (7185.6 cm^{-1}) and 1343 nm (7444.4 cm^{-1}) used in this work. The length and diameter of the C-lens are 20 mm and 3.8 mm, respectively. The working distance and beam divergence of the C-lens are 700 mm and 0.82°, respectively. This results in a beam spot with the diameter of 2.86 mm over a working distance of 1000 mm. Such a small beam spot under-fills the receiving unit, thus ensuring it is fully detected with a good signal intensity. The emitted laser beam was reflected by the right-angle prism with a leg dimension of 5 mm and propagates through the aperture with a diameter of 4 mm. The miniaturized adjusting mirror mount is spring-loaded, with precision alignment screws (M1.6 × 10 mm) to finely align the laser beam in two dimensions within ±5°. The base mount is mounted to a customised enclosure via two neighbouring M2 × 5 mm cap screws, sustaining long-term alignment under variable operating conditions.

The receiving unit consists of a plano-convex lens, a PIN photodiode, a Trans-Impedance Amplifier (TIA) circuit and a base mount. The diameter of the convex lens is 4 mm, allowing enough tolerance for beam steering in traversing the APU exhaust plume. With a focal length of 5.5 mm, the convex lens focuses the transmitted laser on the 1 mm photosensitive area of the photodiode (Hamamatsu, G12182–010K). This photodiode has good sensitivity at the wavelength range of 900–2100 nm, enabling measurement of multiple absorbing species, e.g. water vapor around 1350 nm in this work and CO2 at 1999 nm[7]. The cap of the photodiode is inserted and fixed by a base mount, while the three PINs of the photodiode are connected to a custom-designed TIA circuit that converts the photodiode current to the required voltage signal. As shown in Fig. 3, the TIA circuit features a gain of 2k and a −3 dB bandwidth of 3 MHz, using an AD8065 (Analog Devices) op-amp, and thus enables the sensor to implement Wavelength Modulation Spectroscopy (WMS), in which the laser wavelength can be modulated at frequencies up to hundreds of kHz for high signal-to-noise ratio (SNR) detection of gas-state parameters [17]. The amplified voltage signal is routed through MMCX connectors to the Data Acquisition (DAQ)

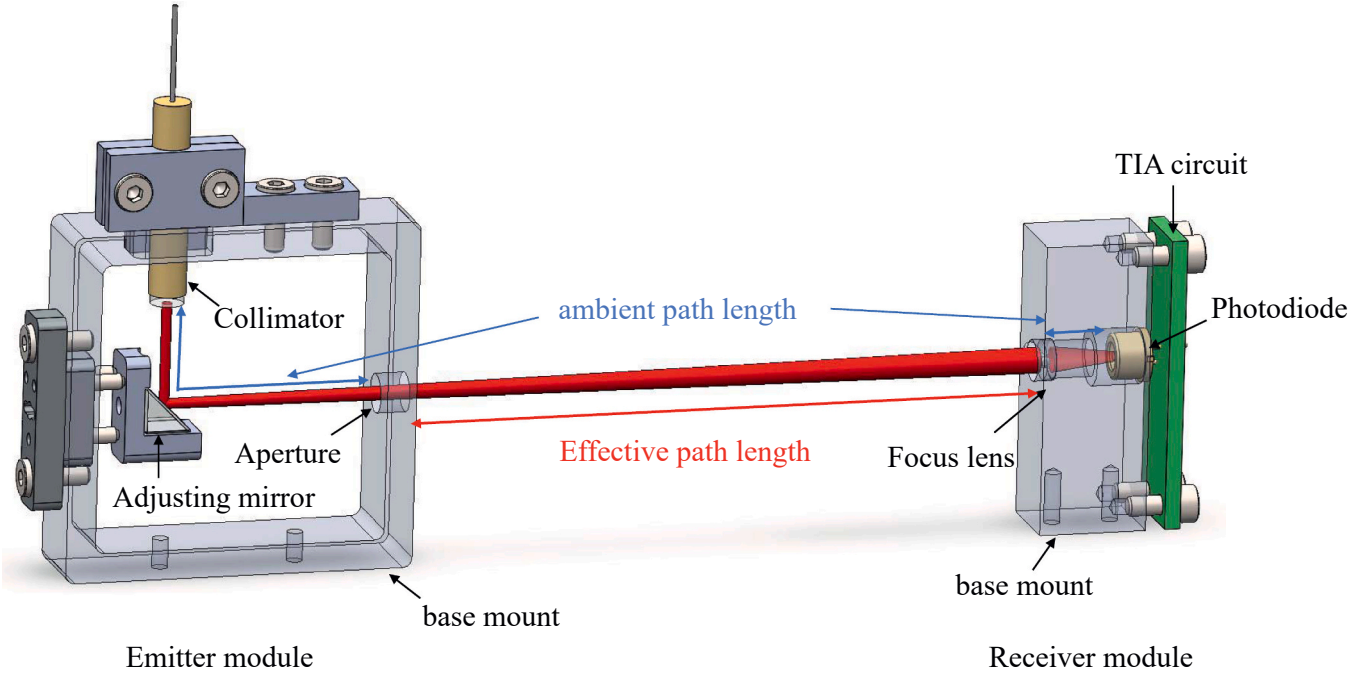

Fig. 2. Design of a laser emitter-receiver unit for the modularized CST sensor.

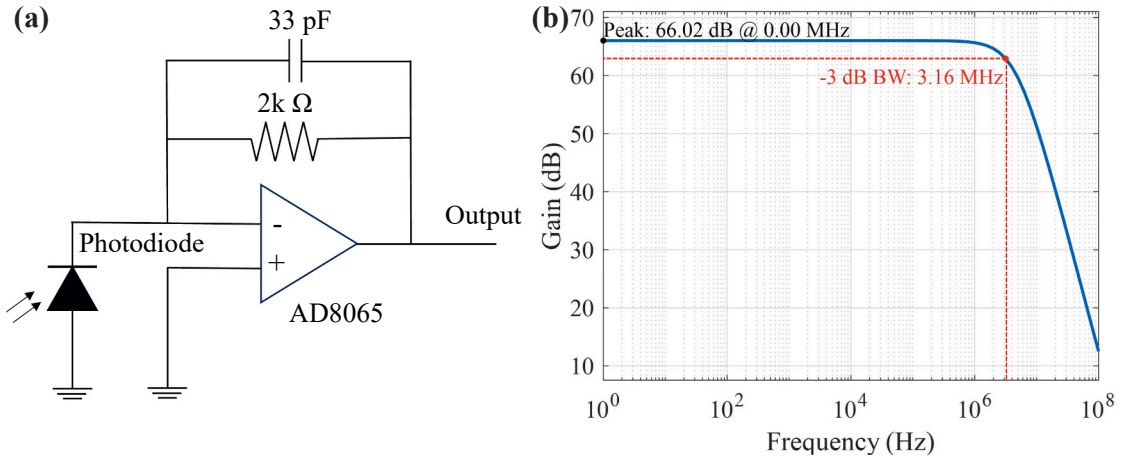

Fig. 3. Schematic diagram (a) the TIA circuit and (b) its frequency response.

system. The receiving unit is also mounted to the customised enclosure via two M2 × 5 mm cap screws.

It is also worth mentioning that the effective laser path length for CST image reconstruction is 807 mm, i.e. from the aperture to the convex lens. However, the additional path length that is within the emitter-receiver unit, i.e. as shown in Fig. 2, also contributes to absorption via ambient water vapor in the LoS measurement, and should be deducted in the signal post-processing stage before image reconstruction.

3.2. Modularized CST sensor assembly

This CST sensor is designed for imaging the exhaust plume of the Honeywell 131–9 A APU with an exit diameter of 254 mm. Considering the downstream expansion of the plume, we set the ROI with a side length l_{ROI} of 310 mm to fully cover the cross section of the plume. The ROI is penetrated by 128 laser beams arranged in four projection angles, 0°, 45°, 90°, 135°. Within each projection angle, 32 equi-spaced emitter-receiver units, with a 10 mm beam spacing, are assembled. This beam arrangement enables the exhaust plume to be uniformly sampled by the parallel laser beams from each projection angle. Given the ROI is meshed into 50 × 50 grid cells, the global spatial resolution in the ROI is 8.1 mm, calculated from the expression $1.306 \times l_{ROI} / 50$ described in our previous work[21]. The 32 emitter-receiver units within a projection are enclosed and fixed on an octagonal Aluminium framework (Fig. 4) to enhance mechanical stability and further protect them from the thermal and vibrational perturbations during the APU test. The modularized design allows ease of maintenance and replacement of individual modules in case of potential misalignment or damage when deployed for the gas-turbine test, possibly for a long period. When adapting the design to image the exhaust of a larger-size gas-turbine engine, the beam distance should be proportionally increased to cover the exhaust plume. In these scenarios, we only need to re-manufacture the enclosures and the octagonal framework, where the same laser emitter-receiver units can be used. This design principle substantially facilitates scaling up and commercializing the CST instruments in turbine exhaust imaging applications.

3.3. Data acquisition system

A modular DAQ system is designed for continuously sampling the 128 transmitted laser beams, developed based on our previously reported quasi-parallel methodology [15]. As shown in Fig. 5, the DAQ system contains 16 synchronized hubs, each working independently for sampling 8 beams. Each hub consists of a signal conditioning circuit (SCC) and an FPGA-based data digitization and processing platform. As indicated in Fig. 6, the SCC is equipped with four independent programmable gain amplifiers (THS7002, Texas Instruments), each conditioning two input laser signals within the analogue-to-digital converters (ADC) maximum allowable input level, i.e., 1 V. The amplified signals are then grouped into two sets of four and time-division multiplexed via two 4-to-1 multiplexers (ADG704, Analog Devices), resulting in two

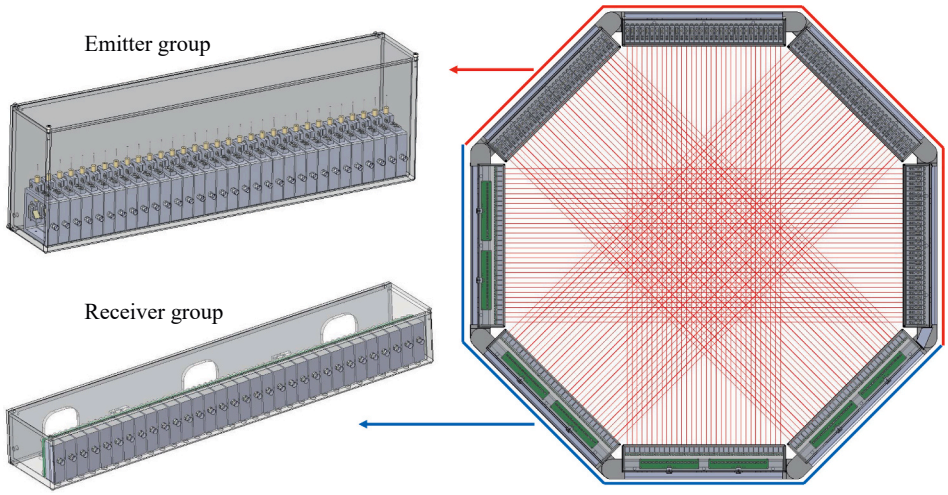

Fig. 4. Assembly of the 128-beam modularized CST sensor for APU exhaust imaging.

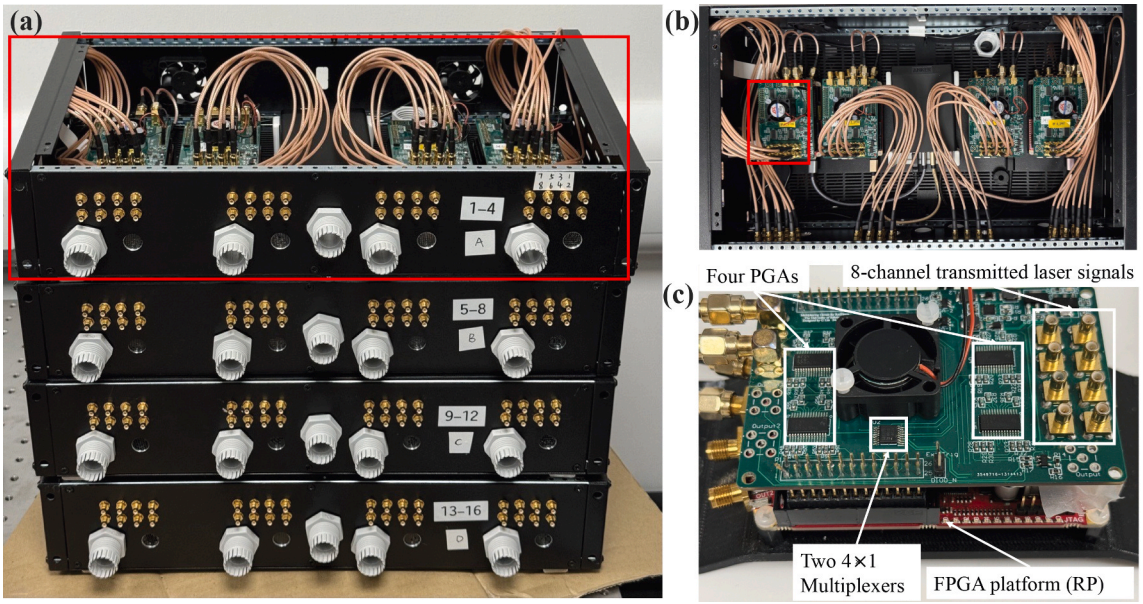

Fig. 5. (a) The 16-hub DAQ system for digitizing the 128-beam CST signals; (b) exposed view of 4 DAQ hubs, handling 32 beam signals, within a single housing; (c) exploded view of a single hub, handling 8 beam signals, as depicted schematically in Fig. 6.

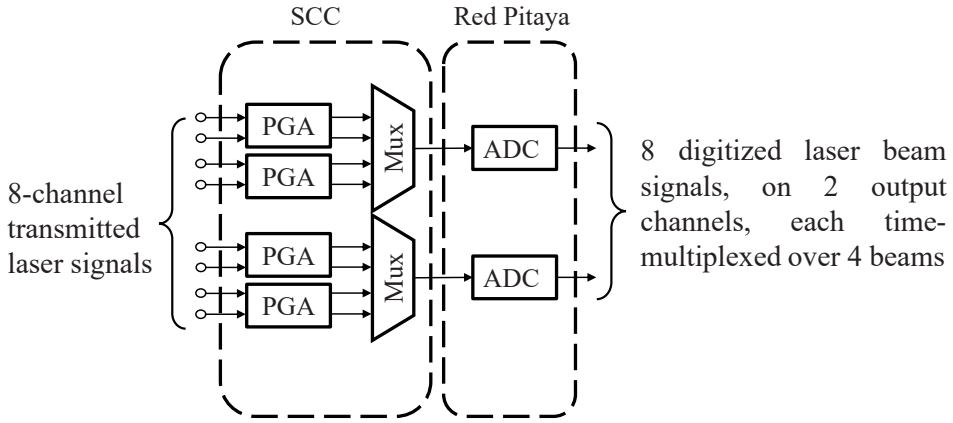

Fig. 6. Flowchart of 8-beam transmitted laser signals on a single DAQ hub, showing the multiplexing, conditioning and digitization steps.

multiplexed analog streams. For example, given a laser scan frequency of 1 kHz, an imaging rate of 250 frames per second (fps) can be achieved using this multiplexing scheme. The two signals are then digitized in parallel using two 14-bit ADCs at 15.625 Mega Samples per second (MSps), which are installed on a commercial FPGA-based digitization and processing platform, Red Pitaya (RP) [22]. The digitized signals are real-time transferred to the workstation via Ethernet at 500 Mbps. The 16 hubs need to transfer the data simultaneously, yielding 8 Giga bits per second (Gbps) total transfer rate. To manage the data communication bandwidth, we adopt two high-speed Ethernet switches (QNAP QSW-M1208–8C), each providing continuous data transfer at 4 Gbps without any loss of data.

4. Lab-scale validation

An overview of the CST system setup is presented in Fig. 7. The emitter and receiver signal flows are indicated by red and blue arrows, respectively. The absorption transitions of water vapor (H_2O) at 7185.6 cm^{-1} and 7444.4 cm^{-1} are used in this work to perform ratio thermometry. The two transitions provide good sensitivity across a temperature range of 300–1800 K [14,23–25], which aligns well with the exhaust gas temperature (EGT) of the APU at different operating conditions [10]. The above transitions are scanned by two distributed feedback (DFB) laser diodes NLK1E5GAAA and NLK1B5GAAA (NTT Electronics), respectively. Each laser diode is temperature- and current-controlled by laser drivers (Wavelength Electronics, LDTC 2–2E). To implement WMS, the injection currents for the lasers are sinusoidally scanned at 1 kHz and modulated at 188 kHz and 250 kHz, respectively. The light emitted by the two laser diodes are frequency division multiplexed and equally split into 128 channels. Each channel is fiber coupled to the C-lens collimator described in the above section. The 128-beam measurements are finally used to reconstruct the temperature and H_2O concentration fields using Tikhonov regularization.

Experiments are conducted to examine the system's performance on capturing various flame profiles. Specifically, two lab-scale burners are used to generate annular and triple flames with distinct spatial characteristics. The diameter of the burner caps ranges from 50 to 80 mm. To accommodate these compact geometries, the central ROI is reduced to 160 × 160 mm^2 in the lab validation, while the out-of-ROI region is regarded as ambient conditions. The downsized ROI enables better resolution of spatial features of the lab-scale flames, and mitigates the rank deficiency that can be caused by reconstructions that include the ambient area. Fig. 8(a) and (b) show the ROI, layout of the burners in the ROI, and key geometric dimensions. The annular burner in Fig. 8(a) is

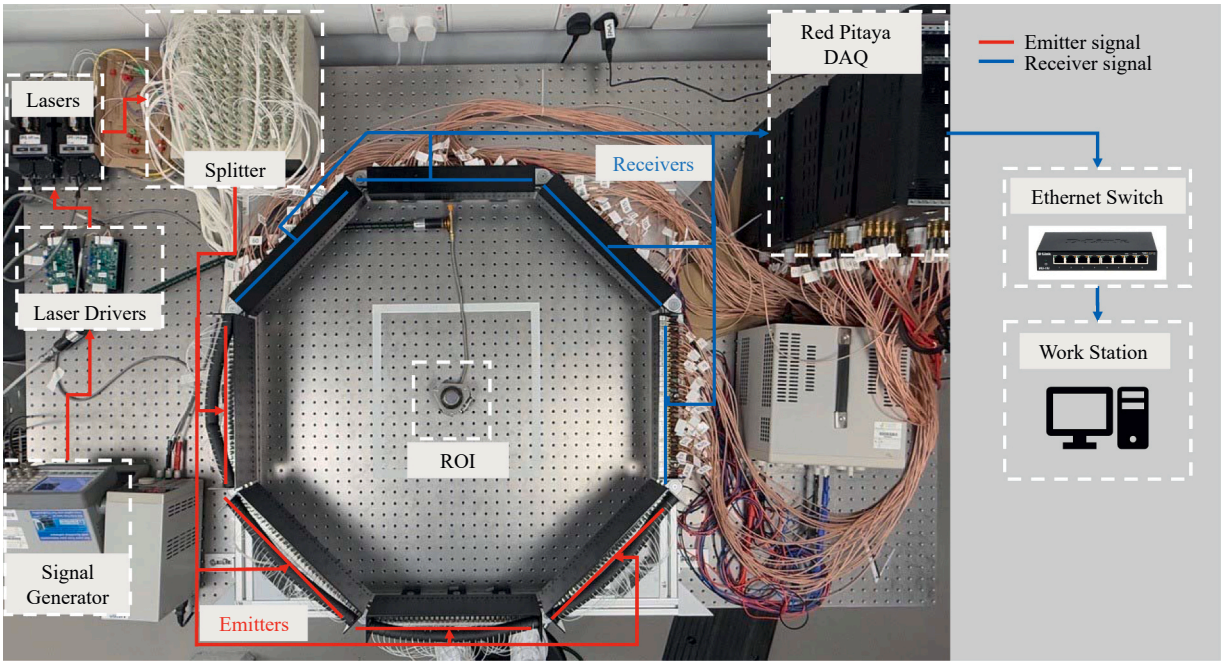

Fig. 7. CST system setup for lab-scale validation.

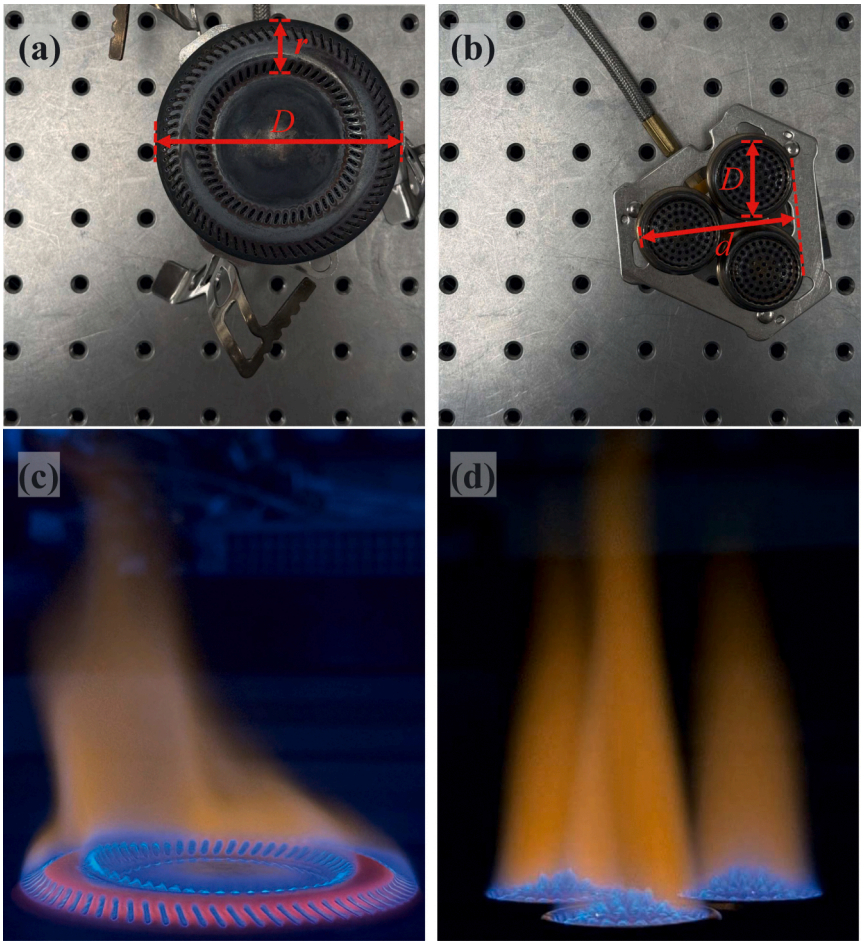

Fig. 8. (a) Annular and (b) triple burners used for lab validation of the CST sensor. (c) and (d) show the flames generated by (a) and (b), respectively.

positioned in the upper-right corner of the ROI and features an 80 mm diameter (D) cap with two concentric rings of fuel outlets. The radial difference between the inner and outer port rings (r) is 15.4 mm. In contrast, the triple burner consists of three identical caps, each with a diameter (D) of 25 mm, featuring evenly distributed fuel outlets. These caps are arranged in a triangular layout with an equivalent side height (d) of 56.4 mm, which is marked in Fig. 8(b). Both burners are fuelled with propane, with flow rates of 2 L/min and 3.6 L/min, respectively. There are holes on the fuel inlets, allowing air to be partially premixed with the propane. Fig. 8(c) and (d) show the photographic flame images captured from the left-hand side of the ROI, in a plane that is nearly perpendicular to the plane of the beam array. Since the propane and air are not perfectly premixed, and do not flow evenly from the outlets of the burner caps, nonuniformity can be observed in the photographs. In Fig. 8(c), the annular flame is stronger on the left edge, corresponding to the upper region of the annular burner in Fig. 8(a). Similarly, in Fig. 8 (d), the rightmost flame appears weaker and shorter, aligning with the lower-right burner cap in Fig. 8(b). These observed non-uniformities are captured by the tomography system and analysed in the following sections. The tomographic measurement plane is located 5 mm above the burner surface. For the analyses presented here, data acquisition is performed over a one-second duration, resulting in 250 reconstructions of temperature and H_2O concentration.

The path-integrated absorption, denoted as A_v in Eq. (2), is obtained by spectral fitting of the 2 f/1 f signal [26]. Fig. 9 shows the mean values and standard deviations (std) of A_v for the 128 beams when measuring the annular and triple flames at the transitions of 7185.6 cm^{-1} and 7444.4 cm^{-1}. In each projection angle, the path-integrated absorption of several laser beams is much stronger than the baseline, indicating their intersections with the flame. The peak values of A_v for the transitions at 7185.6 cm^{-1} and 7444.4 cm^{-1} are about 1.2–2.5 and 8–10 times higher than the baselines, respectively. Due to the high-temperature sensitivity of the 7444.4 cm^{-1} transition, it exhibits stronger absorption in the flame region compared to the 7185.6 cm^{-1} transition. For the annular burner, approximately 10 out of every 32 beams exhibit distinguishable absorption, suggesting a flame diameter of roughly 100 mm. Likewise, for the triple burner, about 7 out of every 32 beams show clear absorption signals, indicating an effective flame region of approximately 70 mm. In addition to flame sizing, the spatial distribution of A_v in Fig. 9 offers insight into the internal structure and symmetry of the flames. For the annular burner shown in Fig. 8(a), A_v exhibits similar profiles and relatively uniform peak amplitude across all projection angles, suggesting an approximately symmetric flame distribution. In contrast, the visibly jagged profiles of A_v in Fig. 9(c) and (d), particularly in the first and second projection angles, indicate multiple overlapping flame structures along certain laser beams. This is consistent with the triple burner's geometry, where heat released from adjacent flames may intersect within the ROI.

Fig. 10 presents the two-dimensional temperature and H_2O concentration distributions for the two flames reconstructed using the 128-beam A_v values averaged over one second. The reconstructions exhibit strong agreement with the expected flame features, accurately capturing flame positions, geometric dimensions, and non-uniformity.

For the annular burner, both the reconstructed temperature and H_2O concentration distributions shown in Fig. 10 (a) and (b), respectively, have an annular structure located in the upper-right quadrant of the ROI. The peak temperature and H_2O concentration are 1127.4 K and 0.059, respectively. The vertical asymmetry of the reconstructions, particularly that shown in Fig. 10 (b), reflects the non-uniformity of the flame observed in the photograph in Fig. 8(c), where the flame intensity is visibly stronger on its left edge.

For the triple burner, the reconstructions shown in Fig. 10 (c) and (d) clearly reveal three hot spots in a triangular configuration. The red-labelled points A, B, and C in Fig. 10 (c) represent the local temperature maxima within the three hot spots. The peak temperature and H_2O concentration at these locations are A (1264 K, 0.041), B (1141 K, 0.036), and C (1279 K, 0.038), respectively. The rightmost hot spot (point B) gives the lowest temperature and H_2O concentration, corresponding to the flame with observed weakest density in the photograph in Fig. 8(d). The internal angles of triangle ABC are measured as $\angle ABC \approx 63.1^\circ$, $\angle BCA \approx 61.2^\circ$, and $\angle CAB \approx 55.7^\circ$, deviating only slightly from an ideal equilateral shape. Additionally, the measured distance d is 54.9 mm, slightly lower than the actual d value of 56.4 mm defined in Fig. 8(b). Comparison between the angles and distance between the real-space and reconstructed positions also tests the spatial resolution of the CST system in practice.

To further quantify the flame structure and stability, Fig. 11 shows the mean and std of the one-second dynamic temperature and H_2O concentration extracted along the horizontal and vertical dashed lines marked in Fig. 10 (b) and (d), respectively. In all subplots, both temperature and H_2O concentration exhibit higher standard deviation at the flame boundaries, compared to those in the flame centre. This is primarily attributed to turbulence and mixing effects at the flame boundary, where enhanced interaction between the fuel and the surrounding ambient air leads to local combustion instability. In contrast, the flame centre exhibits more stable and self-sustained combustion with fuel/air

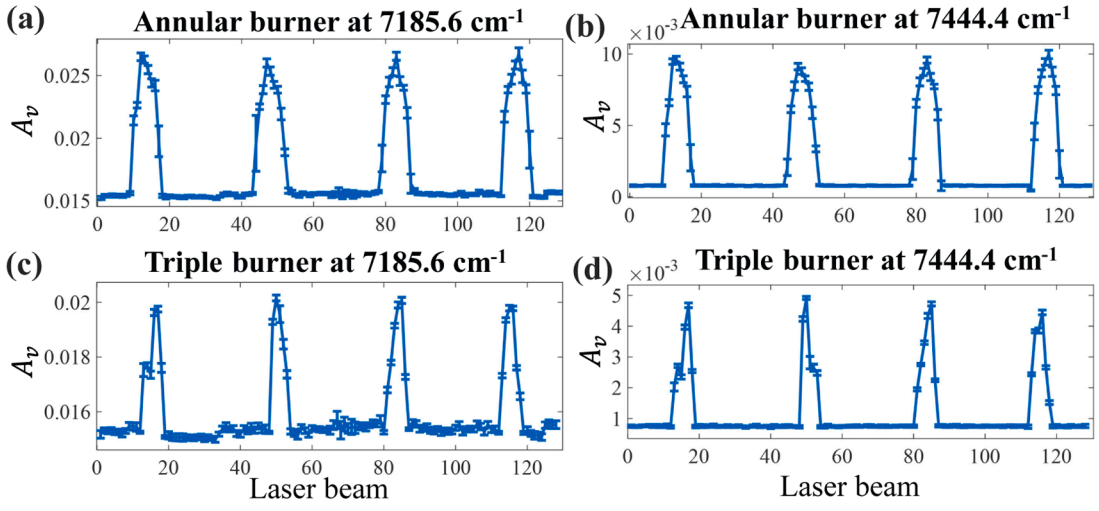

Fig. 9. Means and standard deviations of the path-integrated absorptions at 7185.6 cm^{-1} and 7444.4 cm^{-1} for the 128 laser beams measured on the annular and triple flames.

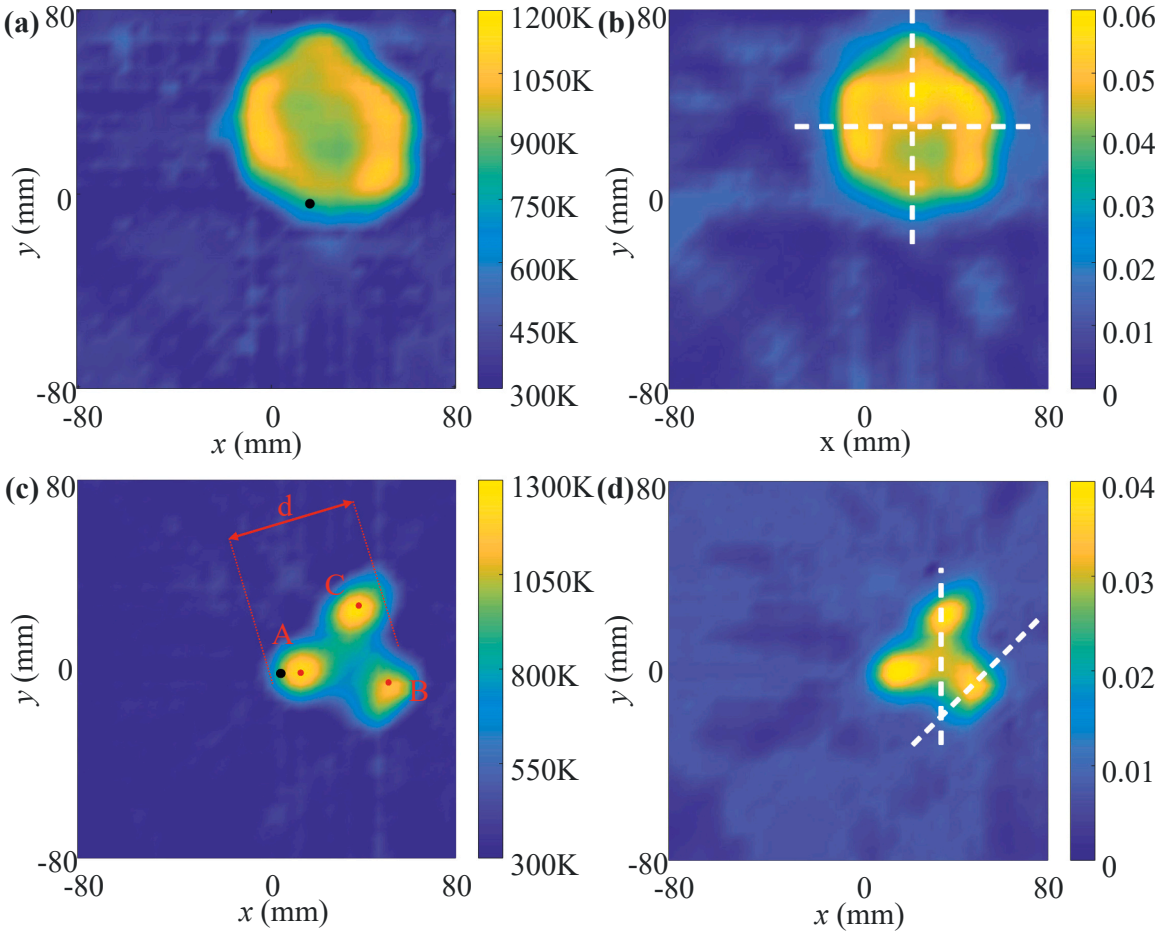

Fig. 10. One-second averaged reconstructions of (a) temperature and (b) H_2O concentration of the annular flame, and (c) temperature and (d) H_2O concentration of the triple flame.

mixture uniformly released from the burner cap.

For the annular burner as shown in Fig. 11 (a) and (b), the reconstructed high-temperature/concentration area, defined as that above 50 % of the full scale, is approximately 88.8 mm for the annular burner, which is slightly larger than the actual burner diameter of 80 mm. This enlargement is mainly due to diffusion and thermal expansion of the flame, as well as the inherent smoothing effects of the Tikhonov regularization. Moreover, the characteristic ring-shaped structure is evident, with the observed radius difference (r) being 16.1 mm, which closely matches the geometric measurement of 15.4 mm in Fig. 8(a).

For the triple burner as shown in Fig. 11 (c) and (d), the reconstructed temperature and H_2O concentration distributions exhibit a main peak and a side lobe in vertical profile and two similar peaks in diagonal profile. The alignment in right peaks across both profiles confirms the symmetry of the upper sub-flame. The width of the high-temperature/concentration region associated with the rightmost peak is approximately 28 mm, slightly larger than the actual burner cap diameter of 25 mm. The side lobe observed in the vertical profile results from partial absorption contributions from adjacent sub-flame plumes, likely due to flame wing overlap or mixing-layer interactions.

To further characterize fluctuation of the flames at their boundaries, the dynamically reconstructed temperature and H_2O concentration are extracted from the flame edges on the black dots in Fig. 10 (a) and (c). Fig. 12 shows the power spectral density (PSD) obtained from the extracted reconstructions and the path-integrated absorption measured from a laser beam penetrating through the black dot. As shown in Fig. 12 (a), the annular flame displays a clear dominant frequency at 9 Hz across all the spectra of the reconstructed temperature, H_2O concentration and the path-integrated absorption. The frequency peak is particularly prominent in all the three spectra, indicating a regular fluctuation likely caused by vortex shedding or periodic flow-flame interactions. In contrast, Fig. 12 (b) shows the triple flame does not exhibit any dominant frequency peak. Instead, the PSD curves appear to be broadband and relatively flat across the 0–120 Hz range. This observation is consistent with our previous experimental findings [27]. This suggests that the triple burner produces a more spatially fragmented or temporally incoherent flame field, potentially due to the independent and uncorrelated behaviour of the three sub-flames.

It can be concluded from the in-lab experiments that the developed CST sensor is effective in resolving both of the experimental gas-state profiles, including two different flame structures and the geometric asymmetries within each structure. For both types of flame structure, the spatial resolution of various features in the reconstructed images is demonstrated to be consistent with the expected performance. In addition, the sensor is capable of identifying dynamic behaviours across different burner configurations under controlled conditions. These in-lab results establish a strong foundation for deploying the system in industrial environments. Building on the validated sensor performance, the next section applies the CST sensor to image the APU exhaust plume.

5. On-site experiment

The on-site experiment is conducted on a commercial APU (Honeywell 131–9 A model), as shown in Fig. 13. The APU is designed with an annular combustor, characterized by a ring-shaped combustion chamber with fuel and air mixing and combustion occurring within the annular

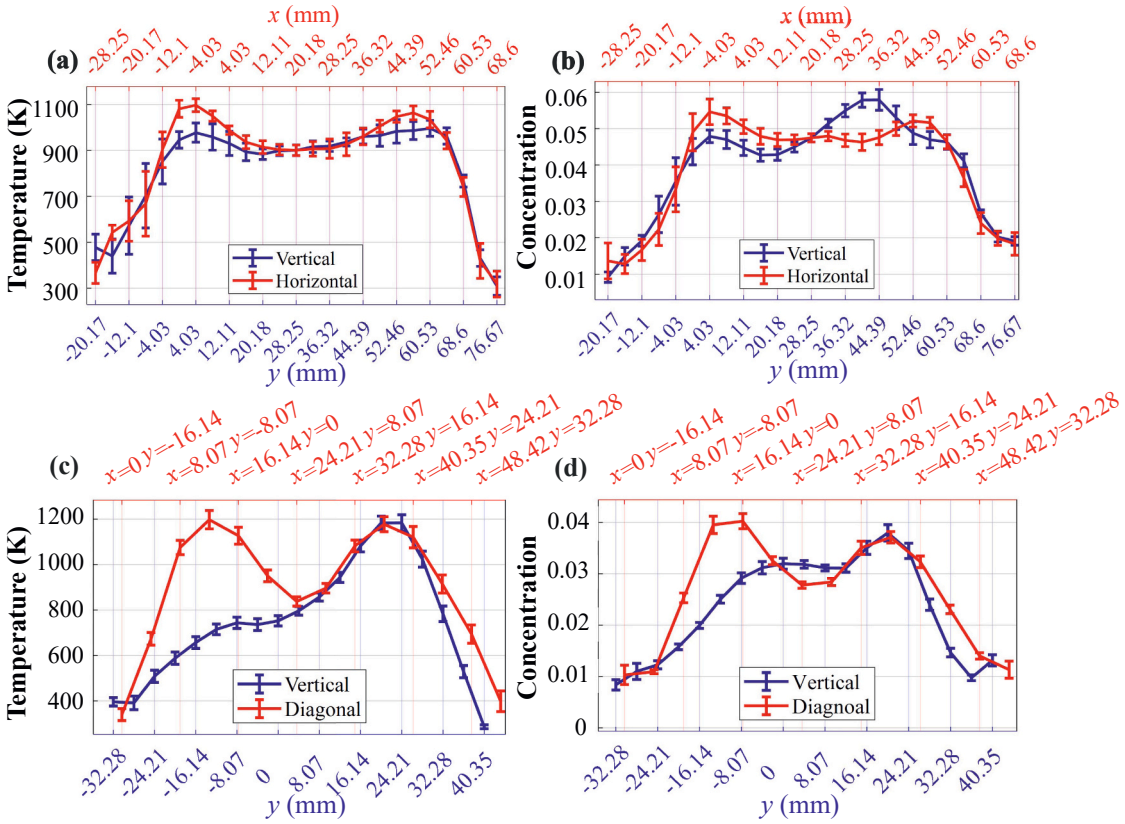

Fig. 11. Profiles along the dotted lines marked in Fig. 10 of (a) temperature and (b) H_2O concentration of the annular flame, and (c) temperature and (d) H_2O concentration of the triple flame.

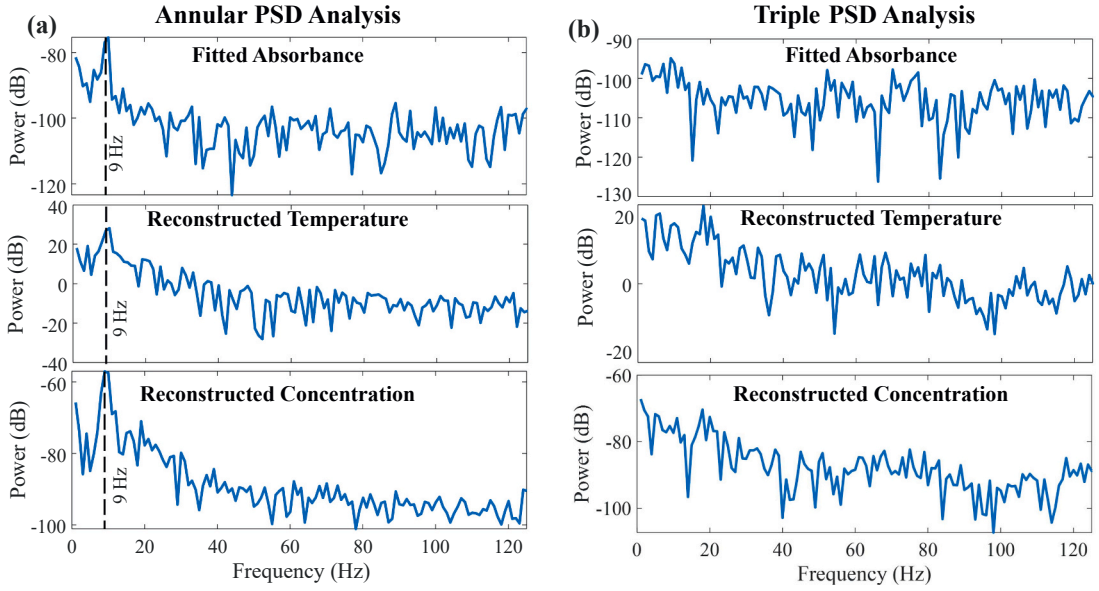

Fig. 12. PSDs on (a) the annular and (b) triple burners.

space. A tube with length of 495 mm and diameter of 254 mm is attached to the APU outlet to guide the exhaust plume to the extraction duct. When the APU is running, thermal expansion can lead to 20–30 mm extension of the tube. Therefore, a CST imaging plane is chosen 45 mm downstream from the tube exit, i.e. 540 mm behind the APU outlet. The APU has a bleed air manifold, taking compressed air from the compressor stage of the turbine stage. In the tests described here, the bleed air is sourced from an external room-temperature compressed air supply. The bleed air is mixed with the combustion exhaust and creates nonuniformity in the imaging plane.

The on-site experimental configuration closely follows that of the laboratory validation. The laser diodes and laser controllers are set up outside the test cell. The generated lasers at 7185.6 cm^{-1} and 7444.4 cm^{-1} are transmitted through 10-meter single-mode fibers and coupled to the 128-channel fiber splitter in the test cell. The 128 collimated laser beams penetrate though the exhaust plume, as shown in

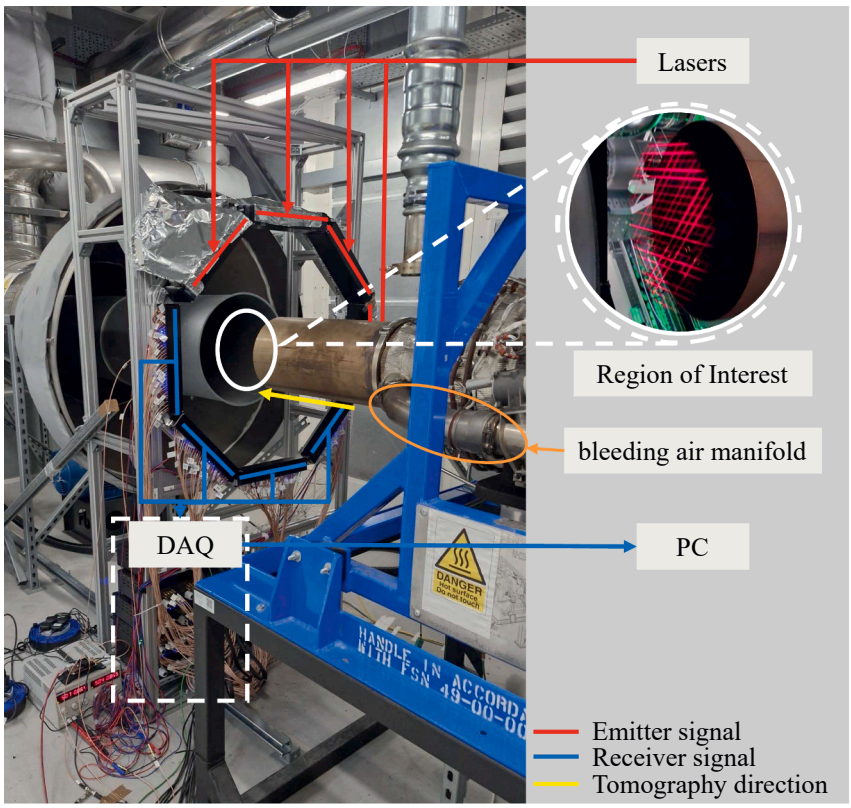

Fig. 13. On-site CST system setup on imaging the APU exhaust plume with beams from two projection angles (out of the four angles, due to the limited intensity of the red laser) are shown in RoI visualization.

Fig. 13, from the emitter ends (marked in red) to the receiver ends (marked in blue). The ROI is defined as a circular cross section with a diameter of 310 mm. The laser transmitted signals are digitized by the 128-channel DAQ system, which is set up beneath the duct. The digitized data are transferred from the DAQ outside the test cell to the Ethernet Switch and saved on the workstation. Since the analogue signal cables from the TIA to the DAQ are all less than 2 m long, exposure to environmental noise in the APU test environment is minimized, enabling high-fidelity CST signals to be obtained. Meanwhile, the telecommunication band fibers and Ethernet Cables enable long-distance and high-quality transfer of the optical and digitized signals. Such a scheme would also be greatly beneficial for CST measurement on larger-scale gas turbines, where the engine test cell can be tens of meters away from the control room.

The experiment uses a Honeywell 131–9 A APU, burning Jet-A1 kerosene in the Ready-To-Load (RTL) condition, where bleed-air demand is zero and all pneumatic valves are shut. To prevent unnecessary compressor work, the intake gate valve was closed. The remaining compressor discharge is dumped directly into the exhaust, producing a distinctive asymmetric plume in which one side is cooler and nearly free of combustion products at the APU outlet. The test lasts for three minutes, during which the laser beams are well aligned with minimal sensitivity to mechanical vibrations introduced in the test cell. This demonstrates strong mechanical robustness of the designed CST system when operating in real-world harsh environments.

Fig. 14 illustrates the performance of the WMS-based CST signal processing under the RTL condition of the APU exhaust test. Specifically, Fig. 14 (a) shows the raw laser transmission of one representative beam across four consecutive scans in 4 ms, while Fig. 14 (b) and (c) display the corresponding $2f/1f$ signals at 7185.6 cm^{-1} and 7444.4 cm^{-1}, respectively. During this period, the APU operates in a thermally stabilized RTL mode, and the exhaust plume maintains relatively steady gas-state parameters. Nevertheless, the raw signal in Fig. 14 (a) exhibits pronounced noise, primarily attributed to turbulence-induced beam

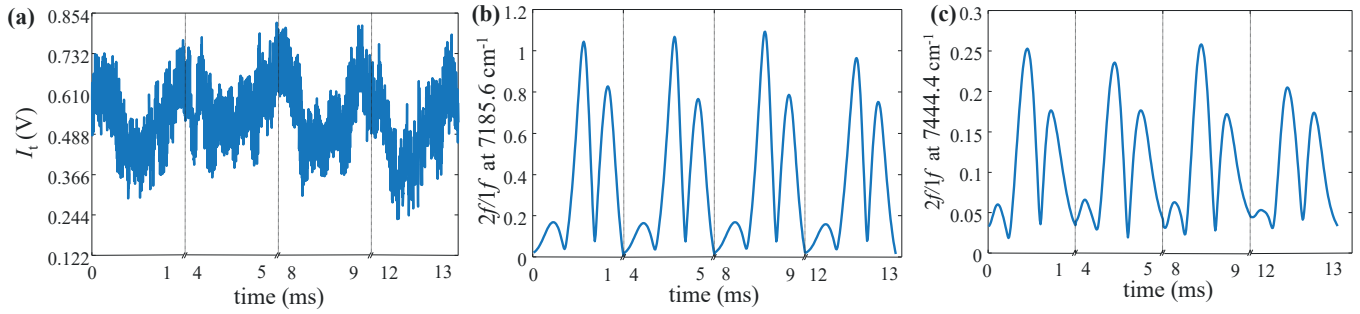

Fig. 14. Four-consecutive-scan laser transmission of a laser beam penetrating the APU exhaust. (a) shows the TDM raw laser transmissions. (b) and (c) show the demodulated $2f/1f$ signals centred at 7185.6 cm^{-1} and 7444.4 cm^{-1}, respectively.

steering, thermal background radiation, and mechanical vibration inherent to the harsh test environment. The demodulated 2 f/1 f signals in Fig. 14 (b) and (c) demonstrate the robust noise rejection capability of WMS, effectively extracting the harmonic signal components from the underlying disturbances. Notably, the harmonic signals exhibit strong consistency across consecutive scans, confirming the temporal stability of the exhaust gas conditions during the measurement period. These results validate the CST system's ability to deliver high-fidelity data in real-world operating environments.

Fig. 15 presents the mean values and standard deviations of 128-beam path-integrated absorption from one-second APU measurement (250 frames). For every projection angle, approximately 27 beams pass through the target flow with distinguishable absorption, suggesting a plume size of around 270 mm. The peak values of A_v for the transitions at 7185.6 cm^{-1} and 7444.4 cm^{-1} are about 2.5 and 9 times higher than the baselines, respectively. Compared to the laboratory results in Fig. 9, the standard deviations in Fig. 15 are more significant due to the stronger turbulence in the APU exhaust plume. As shown in Fig. 15 (a) and (b), the averaged standard deviations for the 7185.6 cm^{-1} and 7444.4 cm^{-1} transitions are 4.7×10^{-4} and 7.6×10^{-5} for ambient beams, and 1.7×10^{-3} and 7.65×10^{-4} for beams that penetrate the APU exhaust plume, respectively. The comparable standard deviations for the lab annular burner for the 7185.6 cm^{-1} and 7444.4 cm^{-1} transitions are 2.4×10^{-4} and 1.0×10^{-4} for ambient beams, and 5.9×10^{-4} and 4.0×10^{-4} for beams penetrating the flame.

Fig. 16 shows the distributions of temperature and H_2O concentration reconstructed using one-second-averaged measurement data under no-load conditions. The exhaust plume exhibits a maximum temperature of 580 K and peak H_2O concentration of 0.0316, both on the left side of the image. The reconstructions display an annular high-temperature/concentration region, corresponding to the combustion occurring within the annular space. Fig. 17 shows the mean and std of one-second dynamic temperature and H_2O concentration, rolling-averaged with a window size of 10, along the horizontal and vertical dashed lines marked in Fig. 16. In both subplots, higher standard deviations are observed near the flow boundaries, reflecting enhanced turbulence and mixing in the plume region downstream of APU exhaust plume. In contrast, the central region of the plume exhibits lower variability. Both the reconstructed high-temperature and high-concentration regions (defined as that above 50 % of the full scale) span approximately 250 mm, which closely matches the inner diameter of the exit tube (254 mm). The vertical gas-state parameters are more symmetric than the horizonal ones. Due to the existence of the room-temperature bleeding air, the temperature distribution shows a crescent-shaped pattern, with hot spots in the left region and a distinct cold spot on the right. Due to the mixing and swirling of the combustion products in the exhaust from the turbine exit, the H_2O concentration shows a ring-shaped profile with a ring width of 90.3 mm. These results provide proof-of-concept validation of the developed CST system for imaging of the APU exhaust.

6. Conclusion

In this work, we present the design, validation, and application of a modularized 128-beam CST system for tomographic imaging of temperature and H_2O concentration in a commercial turbine exhaust. The sensor features 128 independent emitter-receiver units of novel design, arranged in four projection angles, and a synchronized 128-channel DAQ system of a novel modularized design. When implementing WMS with a wavelength scan at 1 kHz, the CST system achieves an imaging rate at 250 fps. A spatial resolution of 8.1 mm is achieved when customizing the beam spacing to 10 mm. This resolving capability is entirely novel, since the system reported by Upadhyay et al. [7] was based on time-multiplexed data acquisition of 126 beam measurements, achieving only around 1 Hz temporal resolution. The modular sensor design presented here ensures mechanical robustness, ease of maintenance, and scalability across gas turbines of varying scales. The achieved temporal resolution is more than adequate to monitor combustion instabilities arising from operation near the lean limit [8,9] and to characterise engine behaviour during typical load transients. Although higher imaging rates up to 1000 fps can be achieved by reducing beam count at the expense of spatial resolution [28], future work will investigate DAQ improvements to push both limits simultaneously.

Experiments using lab-scale annular and triple flames demonstrate the system's penetrating capability to spatially resolve flame locations and profiles, as well as temporally resolving flame fluctuations. Furthermore, on-site deployment of the CST system on a Honeywell APU turbine further validates its robustness in the harsh environment of a commercial combustion test cell. The proof-of-concept results at a steady state, i.e., no-load condition, indicate that the CST system can reveal nonuniformity and swirling of the exhaust plume, which are important factors to diagnose the engine's health and emissions. In future work, we will carry out more comprehensive experiments on the APU, for example, by imaging the exhaust plume results under various working conditions, and interpret the data to infer APU exhaust plume emissions and dynamics.

CRediT authorship contribution statement

Hugh McCann: Writing – review & editing. **Minqiu Zhou:** Writing –

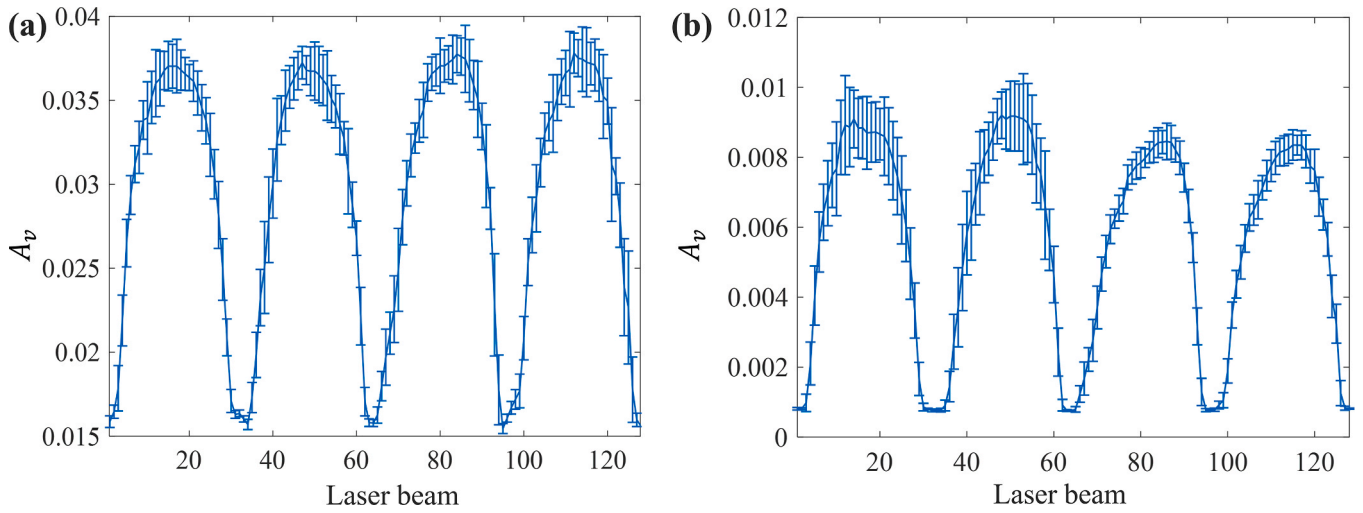

Fig. 15. Path-integrated LoS absorption of 128 beams behind the APU for transitions at (a) 7185.6 cm^{-1} and (b) 7444.4 cm^{-1}.

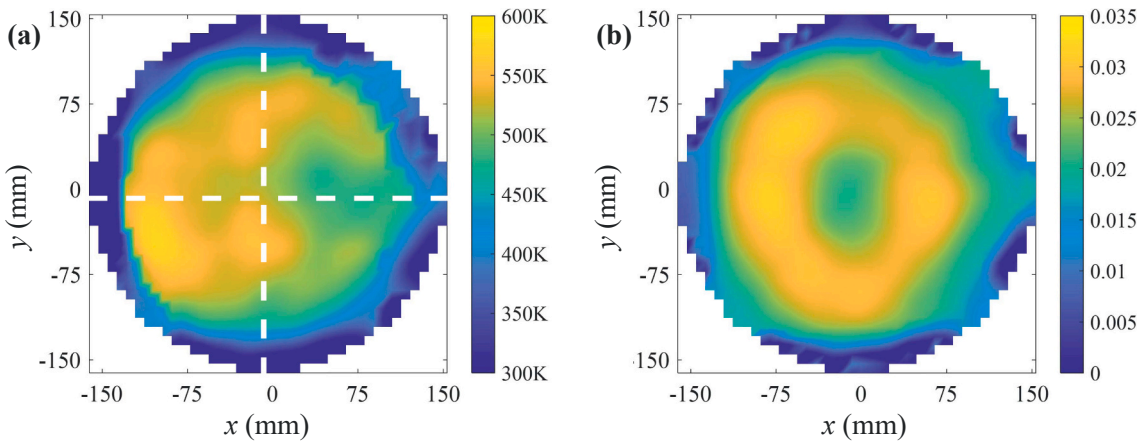

Fig. 16. Distributions of (a) temperature and (b) H_2O concentration reconstructed using one-second-averaged measurement data under no-load conditions.

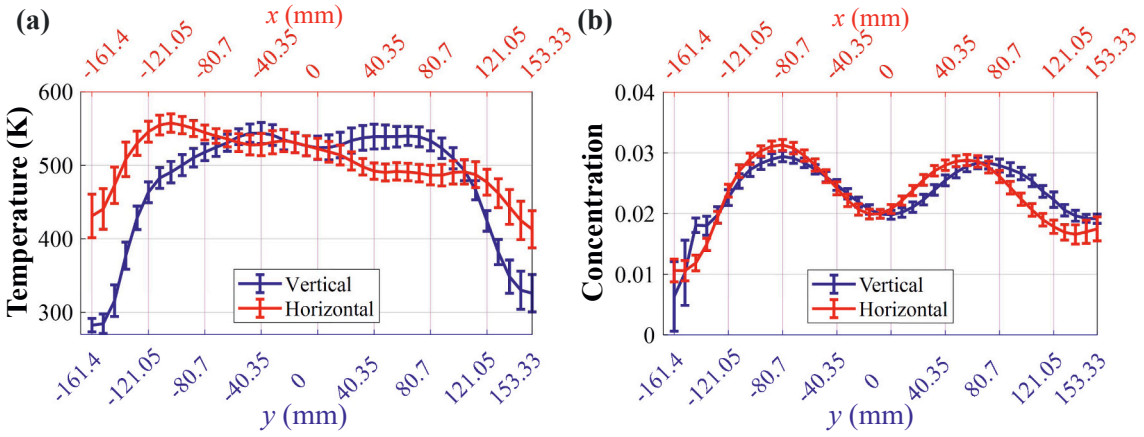

Fig. 17. Profiles along the dotted lines marked in Fig. 16 of (a) temperature and (b) H_2O concentration of the APU exhaust.

original draft, Validation, Investigation, Formal analysis, Data curation. **Chang Liu:** Writing – review & editing, Supervision, Funding acquisition, Conceptualization. **Yikai Xia:** Validation, Resources, Investigation, Data curation. **Rui Zhang:** Resources, Methodology. **Ihab Ahmed:** Writing – review & editing, Investigation. **Yuan Chen:** Validation, Investigation. **Ian Armstrong:** Investigation. **Mohamed Pourkashanian:** Writing – review & editing. **Walter Johnstone:** Writing – review & editing. **Michael Lengden:** Writing – review & editing, Funding acquisition.

Declaration of Competing Interest

The authors declare the following financial interests/personal relationships which may be considered as potential competing interests: Chang Liu reports financial support was provided by Engineering and Physical Sciences Research Council. If there are other authors, they declare that they have no known competing financial interests or personal relationships that could have appeared to influence the work reported in this paper.

Acknowledgements

The authors would like to acknowledge the financial support from EPSRC Programme Grant LITECS (EP/T012595/1).

Data availability

Data will be made available on request.

References

[1] H. McCann, P. Wright, K. Daun, S.J. Grauer, C. Liu, S. Wagner, 5 - chemical species tomography, in: M. Wang (Ed.), Industrial Tomography, second ed., Woodhead Publishing, 2022, pp. 155–205.
[2] W. Cai, C.F. Kaminski, Tomographic absorption spectroscopy for the study of gas dynamics and reactive flows, Prog. Energ. Combust. 59 (2017) 1–31.
[3] S.J. Grauer, A.M. Steinberg, Linear absorption tomography with velocimetry (LATV) for multiparameter measurements in high-speed flows, Opt. Express 28 (22) (2020) 32676–32692.
[4] J. Emmert, H. Schneider, B. Böhm, A. Dreizler, S. Wagner, Phase-locked absorption tomography for retrieving 5 khz time-resolved tracer profiles in solid fuel combustion, Appl. Energy Combust. Sci. 12 (2022) 100093.
[5] K.J. Daun, S.J. Grauer, P.J. Hadwin, Chemical species tomography of turbulent flows: discrete ill-posed and rank deficient problems and the use of prior information, J. Quant. Spectrosc. Radiat. Transf. 172 (2016) 58–74.
[6] R.J. Tancin, R.M. Spearrin, C.S. Goldenstein, 2D mid-infrared laser-absorption imaging for tomographic reconstruction of temperature and carbon monoxide in laminar flames, Opt. Express 27 (10) (2019) 14184–14198.
[7] A. Upadhyay, et al., Tomographic imaging of carbon dioxide in the exhaust plume of largecommercial aero-engines, Appl. Opt. 61 (28) (2022) 8540–8552.
[8] C. Liu, Z. Cao, Y. Lin, L. Xu, H. McCann, Online cross-sectional monitoring of a swirling flame using TDLAS tomography, IEEE Trans. Instrum. Meas. 67 (6) (2018) 1338–1348.
[9] L. Zheng, J. Cronly, E. Ubogu, I. Ahmed, Y. Zhang, B. Khandelwal, Experimental investigation on alternative fuel combustion performance using a gas turbine combustor, Appl. Energy 238 (2019) 1530–1542.
[10] R. Zhang, et al., A fast sensor for non-intrusive measurement of concentration and temperature in turbine exhaust, Sens. Actuators B Chem. 396 (2023) 134500.
[11] C. Liu, H. McCann, L. Xu, Perspectives on instrumentation development for chemical species tomography in reactive-flow diagnosis, Meas. Sci. Technol. 34 (12) (2023) 121002.
[12] W. Zhao, et al., A WMS based TDLAS tomographic system for distribution retrievals of both gas concentration and temperature in dynamic flames, IEEE Sens. J. 20 (8) (2020) 4179–4188.

[13] L. Ma, et al., 50-kHz-rate 2D imaging of temperature and H2O concentration at the exhaust plane of a J85 engine using hyperspectral tomography, Opt. Express 21 (1) (2013) 1152–1162.
[14] R. Zhao, et al., Rapid online tomograph in non-uniform complex combustion fields based on laser absorption spectroscopy, Exp. Therm. Fluid Sci. (2023) 110930.
[15] G. Enemali, R. Zhang, H. McCann, C. Liu, Cost-Effective Quasi-Parallel sensing instrumentation for industrial chemical species tomography, IEEE Trans. Ind. Electron. 69 (2) (2022) 2107–2116.
[16] A. Farooq, A.B.S. Alquaity, M. Raza, E.F. Nasir, S. Yao, W. Ren, Laser sensors for energy systems and process industries: perspectives and directions, Prog. Energ. Combust. 91 (2022) 100997.
[17] C.S. Goldenstein, R.M. Spearrin, J.B. Jeffries, R.K. Hanson, Infrared laser-absorption sensing for combustion gases, Prog. Energ. Combust. 60 (2017) 132–176.
[18] K.J. Daun, Infrared species limited data tomography through tikhonov reconstruction, J. Quant. Spectrosc. Radiat. Transf. 111 (1) (2010) 105–115.
[19] C. Wei, K.K. Schwarm, D.I. Pineda, R.M. Spearrin, Volumetric laser absorption imaging of temperature, CO and CO2 in laminar flames using 3D masked tikhonov regularization, Combust. Flame 224 (2021) 239–247.
[20] R. Zhang, et al., Miniature modular sensor for chemical species tomography with enhanced spatial resolution, in: Proceedings of the IEEE International Conference on Imaging Systems and Techniques (2023) 1–5.
[21] C. Liu, S. Tsekenis, N. Polydorides, H. McCann, Toward customized spatial resolution in TDLAS tomography, IEEE Sens. J. 19 (5) (2019) 1748–1755.
[22] Red Pitaya. ⟨www.redpitaya.com⟩.
[23] Y. Wang, B. Zhou, C. Liu, Calibration-free wavelength modulation spectroscopy based on even-order harmonics, Opt. Express 29 (17) (2021) 26618–26633.
[24] F. Lu, et al., Precise velocity measurement by using even-symmetric 2f/1f harmonics extracted from up- and down-scanning WMS signal, IEEE Trans. Instrum. Meas. 73 (2024) 1–11.
[25] J. Xia, Y. Xia, D. Xiao, R. Zhang, N. Yu, C. Liu, LAS-on-edge: a real-time laser absorption spectroscopic water vapor sensor on edge computing platforms, Sens. Actuators B Chem. 418 (2024) 136258.
[26] C.S. Goldenstein, C.L. Strand, I.A. Schultz, K. Sun, J.B. Jeffries, R.K. Hanson, Fitting of calibration-free scanned-wavelength-modulation spectroscopy spectra for determination of gas properties and absorption lineshapes, Appl. Opt. 53 (3) (2014) 356–367.
[27] J.P. Molnar, J. Xia, R. Zhang, S.J. Grauer, C. Liu, Unsupervised neural-implicit laser absorption tomography for quantitative imaging of unsteady flames, Combust. Flame 279 (2025) 114298.
[28] J. Xia, et al., FPGA-Accelerated distributed sensing system for Real-Time industrial laser absorption spectroscopy tomography at Kilo-Hertz, IEEE Trans. Ind. Inform. 20 (2) (2024) 2529–2539.

Minqiu Zhou received the B.Eng. degree (First Class Hons.) in Electronics and Electrical Engineering with Information Engineering from the University of Glasgow, U.K., and from the University of Electronic Science and Technology of China, Chengdu, China, in 2021, through a joint degree program. She received the M.Sc. by Research degree in Informatics from the University of Edinburgh, U.K., in 2022. She is currently pursuing a Ph.D. degree at the School of Engineering, University of Edinburgh. Her research interests include laser absorption spectroscopy sensor design for reactive flow diagnostics.

Rui Zhang received the B.Eng. degree (Hons.) in electronics and electrical engineering with management from University of Edinburgh, U.K., in 2019. She received the Ph.D. degree in School of Engineering, University of Edinburgh. Her current research interest is laser absorption spectroscopic sensor design for combustion diagnosis.

Yikai Xia received the B.Eng. degree (Hons.) in electronics and electrical engineering from University of Edinburgh, U.K., in 2023. He is currently pursuing a Ph.D. degree in the School of Engineering, University of Edinburgh. His research interests are focusing on physics-informed laser spectroscopic sensing and imaging.

Yuan Chen received the B.Eng. degree from The University of Sheffield, Sheffield, U.K., in 2017, the M.Sc. degree from The University of Sheffield, Sheffield, U.K., in 2018 and the Ph.D. degree from The University of Edinburgh, Edinburgh, U.K., in 2022. He is currently a postdoctoral researcher in the Agile Tomographic Imaging Group at the Institute for Image, Data and Communications, University of Edinburgh, United Kingdom

Ihab Ahmed is working as a research associate at the University of Sheffield, where he is currently pursuing a Ph.D. degree in Future Gas Turbine Combustion. Ihab has gained extensive experience in studying the effects of alternative fuels on combustion and emissions. His research interests also encompass combustor design, fuel delivery systems and combustion dynamics.

Mohamed Pourkashanian is the managing director of the Translational Energy Research Centre and head of Energy2050 and energy research at The University of Sheffield. He has completed numerous major research projects on CCUS clean energy technology and received substantial grants from the EPSRC, EU, NATO and industry. He has published over 400 refereed research papers and is a member of numerous international and national scientific bodies.

Ian Armstrong received the B.Eng. (First Class Hons.) degree in electronic and electrical engineering from the University of Strathclyde, Glasgow, U.K., in 2001, and the Eng.D. degree from the University of Strathclyde in 2006. He is working as a Research Fellow at the Centre for Microsystems and Photonics, University of Strathclyde, developing TDLS-based gas detection systems in the near- and mid-IR spectral regions.

Michael Lengden is a professor in the Centre for Microsystems and Photonics in the EEE department at the University of Strathclyde, Glasgow, U.K. He is engaged in research into high-temperature and high-pressure gas composition measurements using TDLS for harsh environments, such as aero-engine exhausts, mid-pressure liquid fuel combustion rigs, and solid oxide fuel cells.

Walter Johnstone is the Research Professor of Photonic Systems in the Department of Electronic and Electrical Engineering (EEE) at the University of Strathclyde. He is responsible for leading research in the field of applied laser spectroscopy for gas measurements in extreme environments, such as gas turbine aero-engines. Prior to his current position, he held senior management posts as Deputy Head then Head of Electronic and Electrical Engineering (2006–11) and Vice Dean (Research) of the Faculty of Engineering (2001–16).

Hugh McCann is Professor of Tomographic Imaging at The University of Edinburgh, U.K., where he was Head of the School of Engineering (2013–18). He was Professor of Industrial Tomography (1996–2013) at the University of Manchester, Manchester, U.K., following ten years in R&D at the Royal Dutch/Shell Group. He has extended industrial tomography to provide specific chemical contrast using high-speed all-opto-electronic techniques, and has developed electrical impedance tomography for medical applications. He was the Head of the School of Electrical and Electronic Engineering at Manchester (1999–2002), and Chair of the U.K. Professors and Heads of Electrical Engineering (2003–05). Prof. McCann was elected a Fellow of the Royal Academy of Engineering in 2009 and a Fellow of the Royal Society of Edinburgh in 2015. In 2018 he was appointed Honorary Professor at Beihang University, Beijing, China.

Chang Liu received the Ph.D. degree in testing, measurement technology, and instrument from Beihang University, China, in 2016. From April 2016 to January 2018, he was a Post-Doctoral Researcher with the Department of Air Pollution and Environmental Technology, Empa, Switzerland. He is a Senior Lecturer in Optical Sensing and Imaging with the School of Engineering, University of Edinburgh, U.K. His current research interests include laser absorption spectroscopy, active/passive optical tomography techniques and system design, and their applications to reactive-flow diagnosis and environmental monitoring.